ADVANCED MATERIALS
www.advmat.de

# Additive Manufacturing of Poly(phenylene Sulfide) Aerogels via Simultaneous Material Extrusion and Thermally Induced Phase Separation

*Garrett F. Godshall, Daniel A. Rau, Christopher B. Williams,* and Robert B. Moore**

**Additive manufacturing (AM) of aerogels increases the achievable geometric complexity, and affords fabrication of hierarchically porous structures. In this work, a custom heated material extrusion (MEX) device prints aerogels of poly(phenylene sulfide) (PPS), an engineering thermoplastic, via in situ thermally induced phase separation (TIPS). First, pre-prepared solid gel inks are dissolved at high temperatures in the heated extruder barrel to form a homogeneous polymer solution. Solutions are then extruded onto a room-temperature substrate, where printed roads maintain their bead shape and rapidly solidify via TIPS, thus enabling layer-wise MEX AM. Printed gels are converted to aerogels via postprocessing solvent exchange and freeze-drying. This work explores the effect of ink composition on printed aerogel morphology and thermomechanical properties. Scanning electron microscopy micrographs reveal complex hierarchical microstructures that are compositionally dependent. Printed aerogels demonstrate tailorable porosities (50.0–74.8%) and densities (0.345–0.684 g cm$^{-3}$), which align well with cast aerogel analogs. Differential scanning calorimetry thermograms indicate printed aerogels are highly crystalline (≈43%), suggesting that printing does not inhibit the solidification process occurring during TIPS (polymer crystallization). Uniaxial compression testing reveals that compositionally dependent microstructure governs aerogel mechanical behavior, with compressive moduli ranging from 33.0 to 106.5 MPa.**

## 1. Introduction

Aerogels are a unique class of materials comprised of a solid network phase and a porous air-filled phase. These materials boast high porosities and surface areas, combined with low densities and typically low thermal conductivities.[1,2] Aerogels are attractive materials for various applications including mass reduction of parts, thermal insulation, passive solar insulation, absorption, filtration, drug delivery, and biomedical scaffolding, among many others.[1] Aerogels have been fabricated from silica and other inorganic materials,[3] as well as synthetic[1,2] and bio-based polymers,[4] metals,[5] and carbon[6] using a variety of processing methods including sol–gel processing,[7] chemical cross-linking,[8] freeze-templating,[6] and phase inversion.[9,10]

Traditionally, aerogels are processed via casting routes, which limit the processed geometries to monolithic primitive shapes that may then be machined to the desired final form via subtractive machining. A recent evolution of aerogel processing is the use of additive manufacturing (AM), which allows for geometrical customization and the expansion of structural complexity of the inherently lightweight microporous bodies. Specifically, AM of aerogels affords the realization of parts with hierarchical porosity, wherein the aerogel structure provides stochastic nano/microporosity, and the printing process enables tailoring of the meso/macroscale porosity via part design and layered processing. In addition, AM of aerogels could afford the opportunity to directly and conformally deposit the aerogel onto a conventionally manufactured substrate.

Generally, fabrication of aerogels via AM has been accomplished through one of three manufacturing modalities: material extrusion (MEX) of gels and pastes (also referred to as direct ink write, DIW), material jetting (MJT), and vat photopolymerization (VP).[6] Due to strict viscosity constraints imposed by MJT and VP, which specifically require low viscosities (<10 Pa s),[11] DIW is a common route for printing aerogel precursor resins. In DIW, liquidous inks are selectively extruded through a nozzle moving on a defined toolpath, and three-dimensional parts are constructed in a layer-wise process.[11] One major benefit of DIW is its ability to

G. F. Godshall, R. B. Moore
Department of Chemistry
Macromolecules Innovation Institute
Virginia Tech
Blacksburg, VA 24061, USA
E-mail: rbmoore3@vt.edu

D. A. Rau, C. B. Williams
Department of Mechanical Engineering
Macromolecules Innovation Institute
Virginia Tech
Blacksburg, VA 24061, USA
E-mail: cbwill@vt.edu

The ORCID identification number(s) for the author(s) of this article can be found under https://doi.org/10.1002/adma.202307881



**DOI: 10.1002/adma.202307881**

process a wide range of ink viscosities (>10 000 Pa s in shear-thinning fluids),[12,13] including those loaded with various polymers,[14,15] metals,[16] ceramics,[17] eutectic materials,[18] and biomaterials.[19] To enable successful printing, the solid–liquid transitions of the ink must be well-understood. During extrusion, the ink must flow as a liquid through the nozzle onto the substrate. Once deposited, the ink should undergo a rapid solidification process whereby the extrudate displays a modulus increase which allows it to maintain its shape and support subsequent layers.[20] Solidification may occur via photopolymerization,[14,15] yield-stress recovery,[21,22] chemical reactivity,[23] or solvent evaporation.[24,25]

Broadly, DIW of a range of aerogels has been achieved by printing inks containing solvent to produce solvated green parts. Printed aerogels are formed once the solvent has been removed from the green parts through common, nondestructive postprocess solvent evacuation techniques such as supercritical $CO_2$ extraction or freeze-drying. Recent work on the DIW printing of aerogels reveals a variety of materials and methods utilized to fabricate porous bodies. Chandrasekaran et al. fabricated carbon aerogels via a sol–gel solidification technique using an aqueous resorcinol-formaldehyde (RF) ink.[26] Solutions were extruded into a solvent bath to prevent ink evaporation and subsequent structural collapse; solidification of printed roads was enabled by yield-stress reformation of the solids in the ink, enabling DIW printing. A curing process initiated the sol–gel cross-linking step of the RF, after which a solvent exchange process and supercritical $CO_2$ drying formed the porous aerogel. Finally, two-step carbonization and etching yielded the activated carbon aerogels, which boasted high surface areas (1894 $m^2\ g^{-1}$) and high capacitance as compared to nonactivated DIW and bulk carbon aerogels. Yao et al. also fabricated carbon aerogels via DIW, using cellulose nanocrystals (CNCs) as the carbon precursor.[27] Briefly, they created aqueous CNC dispersions and also included silica nanospheres to act as porogens. Parts were printed in air and then freeze dried to create aerogels. The printed parts were then carbonized, followed by the chemical removal of $SiO_2$ to create macropores, and finished with a KOH treatment to create nanoscale pores. This yielded a hierarchical porous structure for improved performance as a supercapacitor at low temperatures.

Synthetic polymers have also been fabricated into aerogels via DIW, often using a phase inversion process to yield parts with porous microstructures and complex geometries. Liu et al. utilized a nonsolvent induced phase separation (NIPS) process to create porosity in printed polyimide (PI) aerogels.[28] PI powder was mixed with a good solvent for the polymer (*N,N*-dimethylformamide, DMF) and a poor solvent for the polymer (poly(ethylene glycol), PEG) to form a homogeneous solution. As the ink was deposited, the good solvent volatilized, decreasing the thermodynamic stability of the PI and PEG, eventually leading to microphase separation and solidification of PI domains. After printing, the PEG was removed and the parts were dried, yielding porous PI aerogels boasting high glass transition temperatures ($T_g$ = 315 °C) and high tensile strengths. Interestingly, Di Luca et al. printed a porous poly(ethylene oxide-terephthalate)/poly(butylene terephthalate) (PEOT/PBT) copolymer ink via a thermally induced phase separation (TIPS) process.[29] The copolymer was dissolved in *N*-methyl-2-pyrrolidone (NMP) at 70 °C inside a commercial bioplotter and selectively extruded in a layer by layer fashion. Upon deposition, the solution cools and the system undergoes phase separation, yielding a two-phase PEOT/PBT and NMP microstructure. After printing, NMP was exchanged with a volatile alcohol or water, and the parts were ambiently dried, forming PEOT/PBT aerogels. It was demonstrated that the initial polymer concentration in the ink as well as the drying conditions affected the microstructure.

In this work, the authors present an expansion of available AM-processable aerogel materials. Specifically, the first reported printing of poly(phenylene sulfide) (PPS) aerogels is realized. PPS is an engineering thermoplastic with excellent thermal stability ($T_g$ = 90 °C, $T_m$ = 280 °C, UL 94 Flame Rating = V-0), mechanical properties ($E$ = 3.4 GPa, $\sigma_y$ = 80 MPa), and resistance to many organic solvents.[30,31] PPS is often used as a substitute for metal parts in aerospace and automotive applications where weight reduction and chemical resistance is required.[32,33] Additive manufacturing of PPS has been demonstrated through the use of MEX of molten filament (also referred to as fused filament fabrication, FFF)[34,35] and powder bed fusion (PBF).[36,37] While these approaches have shown the ability to produce dense PPS parts with complex geometries, the inherent melt processing prevents the production of complex PPS aerogel morphologies with intentional microscale porosity.

To enable printing of PPS aerogel, the authors leverage prior research in fabricating PPS[38] and other polymer[39–43] aerogels via a TIPS phase inversion process. In this process, a polymer is premixed with a solvent and brought to high temperatures where polymer–solvent interactions become favorable, and a homogenous polymer solution is formed. Gelation proceeds if an appropriate gelation solvent is selected, where temperature-dependent polymer-solvent interactions promote microphase separation.[44,45] During cooling, the solution becomes thermodynamically unstable, leading to microphase separation into discrete polymer-rich and polymer-poor domains. This process yields a continuous polymeric network imbibed with the gelation solvent, forming a solvated gel.[44–46] Extraction of the gelation solvent leaves behind an air-filled phase, creating a polymeric aerogel. Recently, we have demonstrated that PPS aerogels may be produced using an environmentally friendly, toxically benign gelation solvent, 1,3-diphenylacetone (DPA), yielding robust fibrillar morphologies, low densities, and good mechanical properties.[38]

While previous works have demonstrated simultaneous DIW-TIPS printing of a variety of material systems, this work features printing aerogels from a high-performance polymer with high processing temperatures (>230 °C) that necessitate a custom DIW printing apparatus. The overall aims of this study are to (1) create a generalizable protocol for printing PPS aerogels via DIW, (2) to understand the solidification process dictating the printability of the PPS/DPA system, and (3) to evaluate the effect of polymer composition on the resulting morphological, physical, and mechanical properties of printed PPS aerogels. Furthermore, comparisons between printed PPS aerogels and cast aerogels are also drawn to interpret any influence of the printing process on the physical and mechanical nature of PPS aerogels.

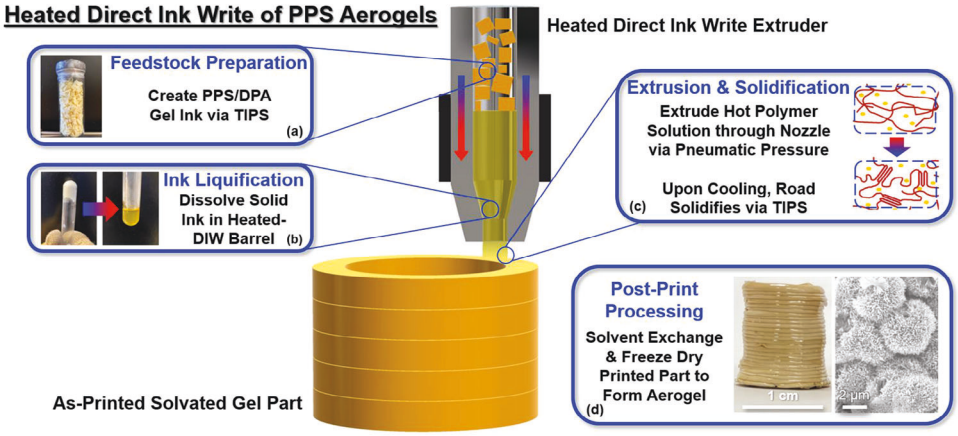


**Figure 1.** A diagram of the heated DIW process. a) PPS/DPA gel is created in a laboratory via TIPS, then broken up and added to the heated-DIW barrel. b) The solvated gel dissolves at the hot end of the barrel, whereby pneumatically pressurized argon gas is used to extrude the polymer solution through a nozzle. c) The printed road cools rapidly and solidifies via TIPS, and parts are then built in a layer-wise fashion. d) The printed gels are solvent exchanged and freeze-dried to create PPS aerogels with a porous, semicrystalline morphology.

## 2. Results and Discussion

### 2.1. Printing PPS Aerogels

PPS solvated gels were successfully printed via selective extrusion of a PPS/DPA gel ink through a custom-designed, heated DIW extrusion system. An annotated diagram of the heated DIW extrusion process is shown in **Figure 1**. To make the ink, PPS is first dissolved into a suitable high boiling point solvent. For this work DPA was selected because it possessed a high boiling point ($T_b = 330$ °C) and it is relatively benign as an FDA-approved food grade additive.[38] Upon forming a homogenous solution at 270 °C, the system was cooled to room temperature, during which it underwent a TIPS process to form a phase separated PPS/DPA solvated gel. This organogel is then easily broken into pellet-sized pieces constituting the gel ink feedstock (Figure 1a) and loaded into the custom-built heated extruder (heated-DIW). Within the lower heating zone, the temperature is raised to form a liquid ink (Figure 1b). With application of pneumatic pressure, the viscous PPS/DPA solution is extruded through the nozzle and deposited upon the print substrate. The extrudate rapidly cools once it contacts the room temperature substrate, at which point it once again phase separates via TIPS and quickly solidifies by crystallization of the PPS component[38] (Figure 1c). Due to the high viscosity of the extrudate and the rapid solidification, the extruded road maintains its shape and is capable of supporting the deposition of subsequent layers as the part is built. After printing, the part is solvent exchanged and freeze-dried to remove the gelation solvent, leaving behind a hierarchically structured, porous PPS aerogel (Figure 1d).

A visual demonstration of the heated-DIW/TIPS printing process is presented for the deposition of a linear bead (**Figure 2**a) and a multilayer cylindrical build (Figure 2d). Initially, the hot PPS/DPA liquid is clear and dark brown in color, but quickly transforms to an opaque and tan solid appearance within seconds after the heated nozzle moves past the deposited bead. This change in visual appearance is attributed to the crystallization/solidification process occurring during the TIPS thermoreversible gelation taking place as the liquid cools and gels. Using an infrared (IR) camera to monitor the temperature of deposited bead during the deposition/build, it is clear that temperatures above 200 °C (i.e., the crystallization temperature for a 30 wt% PPS/DPA system, Figure S1, Supporting Information) are observed as bright yellow/orange pixels only in regions very near the moving nozzle. Moreover, the rapid cooling needed for solidification and structural stabilization during the deposition of multiple layers is apparent in the IR image of the cylindrical part build (Figure 2e).

Using a temperature calibrated IR camera, in situ measurements of the cooling rate of a printed PPS/DPA road may be quantified to evaluate the solidification process during the DIW print. Correlation between the observed cooling rate and thermal transitions of the PPS/DPA solution measured via differential scanning calorimetry (DSC) (Figure S1, Supporting Information) allows for a deeper understanding of the time-dependent processes responsible for the solidification that enables successful DIW printing. Figure 2c presents a plot of temperature versus time of the highlighted pixel of the 30 wt% printed road (Inset of Figure 2c). The cooling rate profile demonstrates that immediately upon deposition, the ink temperature drops from 216 °C to 183 °C within just 0.97 s after extrusion, yielding a cooling rate of −34.0 °C. According to the DSC thermograms, the polymer in the 30 wt% PPS/DPA solution crystallizes at approximately 200 °C at the fastest possible cooling rate available to the DSC used (≈60 °C min$^{-1}$) (Figure S1, Supporting Information). Together, these cooling rate and DSC data indicate that the extrudate spends less than a second in the solution state after deposition, prior to polymer crystallization (≈0.84 s). Consequently, at the extrusion speed of 4 mm s$^{-1}$, the bead is solid at distances of less than 1 mm from the moving print nozzle. After the part cools below ≈183 °C, the cooling rate gradually decreases until the part equilibrates near room temperature, approximately 35 s after deposition. Figure 2d,e demonstrates the ability of the PPS gel ink to solidify fast enough to form stable beads that are needed to create complex parts in a layer-wise fashion. The macro- and microscale origins of this rapid solidification can be explained

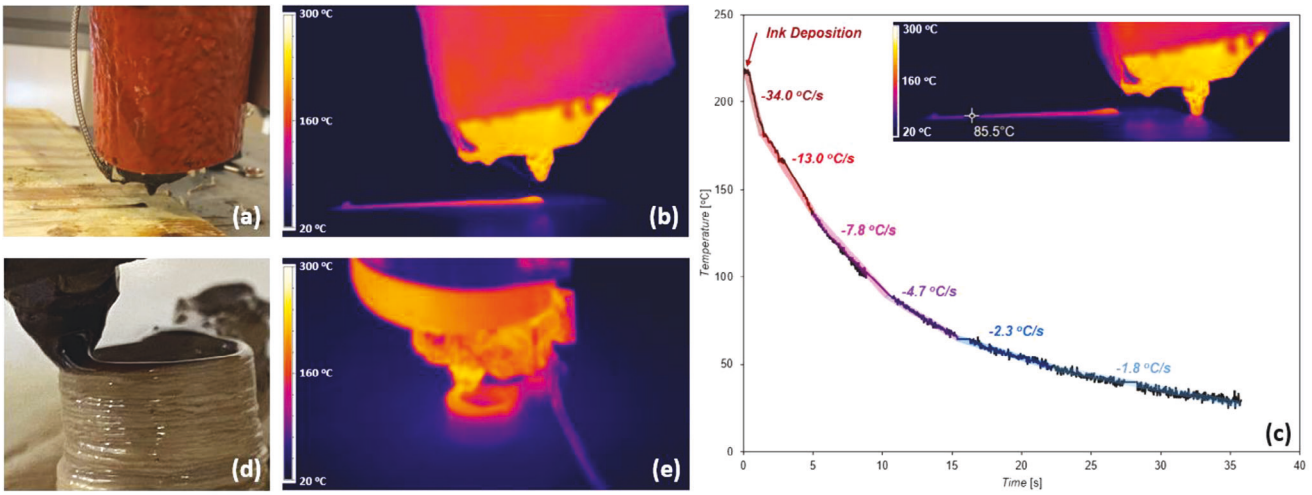


**Figure 2.** a) Digital camera image of in situ DIW printed 30 wt% PPS gel in a single road deposition, with b) the corresponding in situ IR image of the cooling bead, immediately after deposition. c) A temperature versus time profile of the highlighted pixel (pixel area = 17 × 17 µm) of the single road deposition (inset, quantified using the IR camera). d) Digital camera image of DIW printed 30 wt% PPS gel of the multilayer build of a cylindrical part, with e) the corresponding in situ IR image of the cooling layers, during the cylindrical deposition. Extrusion speeds for all depositions were set at 4 mm $s^{-1}$.

through multiple thermal and material factors. A rapid cooling rate of the extrudate containing fast-crystallizing PPS leads to quick solidification upon extrusion. The initial precipitous drop in temperature upon deposition, observed in Figure 2c is related to the low thermal mass of the extrudate and the high temperature gradient between the nozzle and the environment. PPS is a fast crystallizing polymer, with reported isothermal crystallization half times of 3–10 s at temperatures between 160 °C and 200 °C.[47] Therefore, the almost-instantaneous solidification of printed PPS/DPA roads can be explained by the fast drop in temperature, which brings about rapid PPS crystallization.

Tall single-wall cylindrical parts (height = 10–12 mm, OD = 10–12 mm) were also printed, as highlighted in Figure 2d. Figure 2e reveals an in situ IR thermography image capturing the printing of a hollow cylinder used for further physical and mechanical testing. From the IR image, it is clear that heat is retained in the upper two or three layers (approximately 100–140 °C) for 30 to 60 s after being deposited, while the lower layers appear cool to about 60 °C in a few minutes after printing. The deposition speed was set to 4 mm $s^{-1}$ for these experiments, resulting in layer print times of ≈10 s. Residual heat is important for remelting previously deposited layers, which improves interlayer bonding in FFF printing.[48,49] A similar influence of retained heat is thought to occur in PPS/DPA gel printing as well, since the mechanisms of layer solidification (polymer crystallization) and interlayer adhesion (interlayer entanglement) are presumed to be the same as in FFF. Figure 2d,e again reveals that the printed bead begins to solidify so rapidly (<1 s) that the layer transitions to a solid prior to the completion of that layer (layer time estimate = 10 s, translation speed = 4 mm $s^{-1}$). This is unique, as typical DIW inks feature solidification mechanisms with slow solidification rates (i.e., yield stress formation) where lower layers may sag and spread during printing of tall structures. PPS/DPA ink begins to opacify rapidly, indicating solidification (based on previous work on PPS/DPA correlating PPS crystallization and cloud point temperatures[38]). This allows for tall parts of many layers to be printed from the PPS polymer solution.

### 2.2. Printed Aerogel Geometries

A benefit of additive manufacturing aerogels is the ability to maintain porosity on the microscale while tailoring part porosity on the mesoscale and part geometry on the macroscale. This affords the opportunity to tailor aerogel architecture to satisfy specific design requirements and applications. **Figure 3**a,b displays multiple printed parts from both 30 wt% (a) and 50 wt% (b) inks. Printed parts include tensile bars, hexagonal lattices, and cylinders. The heated-DIW system demonstrated the ability to form parts with sharp corners, filled or hollow layers, and curvature. Images of printed cylinders in Figure 3a,b shows high resolution layers (≈0.4 mm layer thickness) with good shape retention afforded by rapid road solidification. Additionally, printed cylinders highlight the ability of heated-DIW to print tall structures of over 25 layers 0.5 mm each in height, indicating that both 30 and 50 wt% PPS/DPA inks possess sufficient gel strength for supporting subsequent layer deposition. Parts do not contain observable macro-scale voids and there is no evidence of delamination between layers, which suggests sufficient interlayer adhesion, likely due to some degree of remelting (as confirmed by the in situ IR thermography) as subsequent layers are deposited. Although rapid polymer crystallization is associated with warping of FFF parts,[50] the presence of solvent within the PPS/DPA extrudate tends to decrease the volume change upon crystallization when compared to a neat polymer, which may explain the lack of shrinkage-induced defects in the gel parts. Some inconsistencies in layer geometry and layer thickness were caused by temperature variations within the barrel, leading to viscosity changes and slight over/under extrusion during a given print. These issues can be remedied through further hardware development.

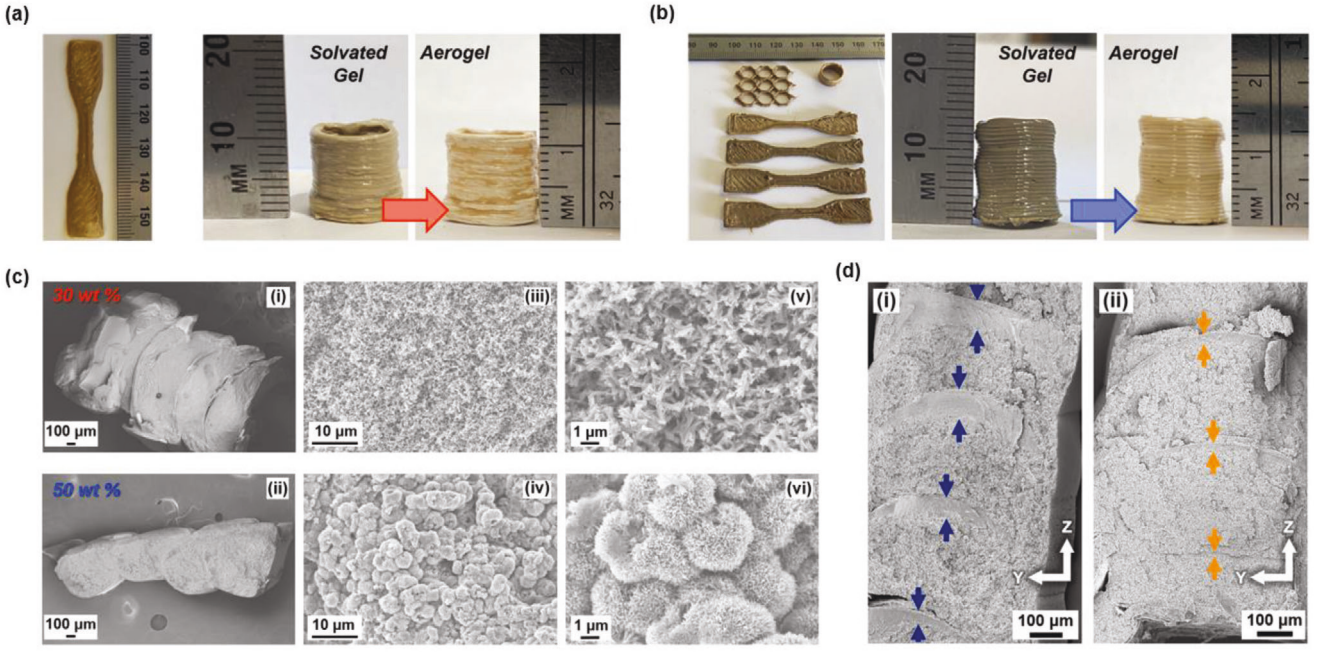


**Figure 3.** Digital photographs of DIW printed PPS gels; a) 30 and b) 50 wt%. c) Scanning electron microscope (SEM) micrographs of printed 30 wt% PPS aerogels ((i), (iii), and (v)), and printed 50 wt% PPS aerogels ((ii), (iv), and (vi)). Magnification increases from left to right. d) SEM micrographs of the cross sections of 50 wt% DIW printed PPS aerogel walls, which were printed with (i) no pause between layer deposition, and (ii) a 15 s pause between layer deposition. Interlayer welds are highlighted between arrows.

After solvent exchange and freeze-drying, printed parts clearly retain their as-printed size and shape. Interestingly, changes in color are observed once the solvated gel is solvent extracted to form the aerogel. The darker color of the solvated gels is due to slight degradation of the solvent at the high extrusion temperatures. Precautions were taken to reduce the residence time of solutions to avoid excess degradation.

### 2.3. Printed Aerogel Morphology

Understanding the morphology of aerogels allows for the development of key process–structure–property relationships that can be used to design microstructures yielding desired properties. Figure 3c highlights SEM micrographs that reveal the morphologies of printed PPS aerogel cylinders. Figure 3c(i),(ii) displays four layer cross-sections of printed cylinders of 30 and 50 wt% inks, respectively. Both samples display smooth outer skins, likely products of rapid cooling and solvent evaporation at the exterior surface once phase separation begins upon ink deposition, as seen in other TIPS systems.[51] The fast cooling rate of the polymer solution in air leads to a concentration gradient at the surface as solvent evaporates; as the quantity of solvent decreases, the porosity of the surface layer decreases as well, forming a skin at the extrudate surface.[51]

Figure 3c(iii)–(vi) reveals the finer textures of the aerogels fabricated from precursor inks featuring 30 and 50 wt% solids, respectively. Aerogels of both concentrations appear highly porous, with visible micron-scale pores created upon the sublimation of ice during the freeze drying process. Nitrogen sorption analysis reveals Brunauer-Emmett-Teller (BET) surface areas of the 30 and 50 wt% printed aerogels to be 178.6 and 109.1 $m^2 g^{-1}$, respectively, as presented in Figure S2 (Supporting Information). These values are high, indicating the presence of nanoscale porosity in both 30 and 50 wt% aerogels which scales inversely with the polymer composition. The surface areas of the printed parts are somewhat lower than those of the 30 and 50 wt% aerogels cast in a laboratory setting (284.5 and 178.6 $m^2 g^{-1}$, respectively; Figure S2, Supporting Information), indicating that the printing process has a modest effect on the nitrogen-accessible surface area of PPS aerogels. The differences between the cast and printed surface areas at each composition are potentially linked to the thick layer interfaces present within the printed aerogels, which are discussed in more detail below. A representative image of a cast PPS aerogel is presented in Figure S3 (Supporting Information).

Interestingly, the morphology of the printed aerogel is highly dependent on the ink concentration. In Figure 3c(iii),(v), 30 wt% PPS aerogels display an isotropic fibrillar morphology. In our previous work,[38] these fibrils have been identified as axialites, which are premature spherulites that form under specific processing conditions, including systems in which the nucleation density is high.[52,53] In contrast, Figure 3c(iv),(vi) reveal spherulitic morphologies of the 50 wt% printed aerogels. The porous surfaces of the spherulites likely originate from solvent which was expelled radially outwards as lamellae crystallize and grow. Upon the removal of such solvent, intraspherulitic porosity was formed.

The influence of polymer composition on microstructure is an important relationship to understand, as the resulting part morphology has implications for its performance. One explanation for the observed morphological difference of the aerogels formed from the different ink concentrations is that a specific

processing parameter, such as printing temperature, is affecting the nucleation density of the inks, whereby the 30 wt% parts display high nucleation densities and thus axialitic morphologies, and the 50 wt% parts with lower nucleation densities are comprised of spherulites. Controlling nucleation density through processing without the addition of nucleation agents has been demonstrated through self-nucleation.[54]

When a semicrystalline polymer is heated above its melting temperature and below its equilibrium melting temperature (i.e., the theoretical melting point for a crystal of infinite thickness), then the polymer melt should be fully amorphous and should not contain any residual crystallinity. However, depending on temperature, there may exist some melt memory, whereby chains still maintain correlations to each other in solution. These correlations, also termed self-nuclei,[54] do not exist in a purely amorphous state nor a purely crystalline state and act as nucleation agents, increasing the nucleation density of the system. When a polymer solution or melt containing these self-nuclei is recrystallized, increased nucleation density typically yields smaller spherulites or even axialites. Inversely, when a solution is dissolved at high enough temperatures to remove self-nuclei, the nucleation density is reduced and larger spherulites form upon crystallization. The presence of self-nuclei has been observed in many polymers[54]; it has specifically been observed in PPS crystallized from both the melt[55,56] and from solution.[53]

Work by Chiang and Lloyd[53] has demonstrated the effect of the dissolution temperature, or the temperature at which a solvated gel is dissolved back into a homogenous solution, on the resulting morphology of thin PPS membranes fabricated via TIPS. Membranes fabricated at higher dissolution temperatures displayed spherulitic morphologies, while those formed at low dissolution temperatures displayed axialitic morphologies, indicating that self-nucleation has a strong affect on the microstructures of PPS membranes. The resulting morphologies of printed 30 and 50 wt% PPS aerogels in this work suggests that self-nucleation may be occurring during the printing process of PPS/DPA. Using the IR camera, the average extrudate temperature of the 30 wt% parts is 208 °C ± 8 °C, while the temperature of the barrel must be raised to extrude the more viscous 50 wt% solutions, resulting in higher extrudate temperatures (243 ± 8 °C). Apparently, the extrusion temperatures required to print the more concentrated ink (50 wt%) are high enough to destroy self-nuclei, producing a spherulitic microstructure upon crystallization. Interestingly, the morphologies of 30 and 50 wt% PPS aerogels formed by a laboratory-scale casting process at the same dissolution temperature presented in Figure S4 (Supporting Information) both reveal axialitic morphologies, confirming that the change in polymer concentration is not responsible for the difference in morphology between the 30 and 50 wt% printed aerogels. These results suggest self-nucleation is responsible for the observed morphological differences between the printed aerogels.

Understanding the effect of printing parameters on the morphology of the interlayer welds of a polymer AM part guides processing conditions to maximize part effectiveness and to create porous microstructures with as few heterogeneities as possible. This understanding also helps to interpret the process physics governing any partial remelting of a previously printed road once the next layer is deposited. Additionally, layer interfaces in AM polymer parts dictate many mechanical properties; increased chain entanglements between layers at the interfaces generally lead to stronger parts.[48,57] Figure 3d highlights results from a simple experiment aimed at probing the effect of pause time taken between the deposition of each layer on the interfaces of a 10 layer 50 wt% PPS gel. Two printed parts were formed from a 1 cm long line toolpath, 10 layers tall, at the same print speed (8 mm $s^{-1}$), pressure (10 psi), and layer height (0.3 mm). However, in one part, no pause was taken between the deposition of successive layers (the cross section for the no-pause part is shown in Figure 3d(i)), while in the other printed specimen a 15 s pause was taken between the printing of each layer (Figure 3d(ii)). This pause time is in addition to the approximately 5 s each layer takes to be deposited. Note, a faster print speed was used in this experiment to isolate the effect of pause time on morphology with less influence of print time. The key result of this comparison is that the interlayer welds, identified between the arrows shown in Figure 3d(i),(ii) are much thicker in the *z*-direction in the part printed without a pause taken between layers. Image analysis indicates that the average interface thickness in the part printed without pause is 81 ± 28 microns, versus 51 ± 31 microns in the part printed with 15 s pauses between layers.

The thicker interfaces for the no-pause part can be explained by the increase in the retained heat (as demonstrated in Figure 2d for a sample printed without pauses). As a layer is printed, it rapidly begins to lose heat and approaches the environmental temperature, as observed in Figure 2c. The next deposited layer then re-melts the previous layer, where polymer chains diffuse at the interface, forming the interlayer weld. Therefore, upon deposition of a given layer, the previously deposited layer is hotter in the part printed without pausing. This aids in remelting that previously printed layer, and thus the part printed without pausing displays thicker interfaces.

In the case of the PPS gels highlighted in Figure 3d, the welds are much less porous than the bulk morphology. Recent simulations of TIPS solutions cooling in the presence of a solid substrate that has good interactions with the polymer demonstrate that polymer chains will preferentially migrate out of solution and form a solid polymeric layer on the substrate.[58] If the dense outer skin of the previously deposited layer acts as the substrate, then upon extrusion of the next layer polymer chains in solution may migrate to this substrate forming a layer of high PPS concentration. This phenomenon may explain the lack of porosity of the interlayer welds between regions of porous aerogel.[58] Additionally, the interlayer regions are much thicker than the exterior skin of both prints (9 ± 3 microns), indicating that remelting is the likely cause of these dense interfaces rather than just an evaporation process that occurs after each layer is deposited.

As further evidence of this heat retention and remelting phenomenon, the interlayer welds of both prints in Figure 3d are thicker towards the top of the part, indicating that the amount of heat retained in the part increases with the introduction of more layers. In situ monitoring of printed parts with an IR camera showed that the minimum temperature each layer reached prior to the deposition of the next layer tended to increase as part height increased. It must be noted that this trend is complex, with the first layers experiencing cooling primarily via conduction to the room temperature build plate, and the upper layers experiencing heat loss through convection to the air. Future work must

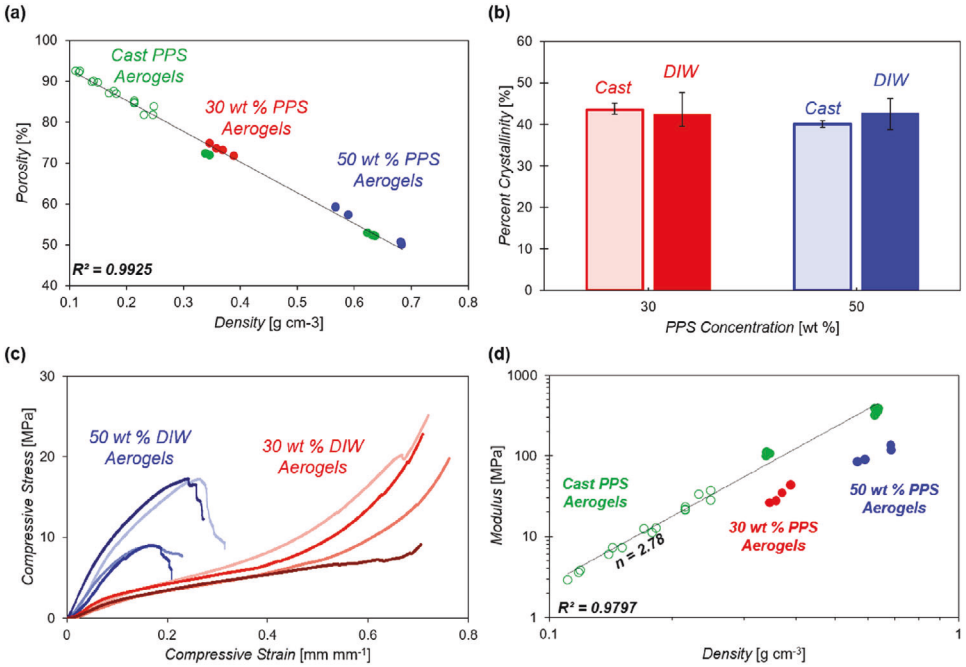


**Figure 4.** a) Porosity versus density of cast and printed poly(phenylene sulfide) (PPS) aerogels. b) Percent crystallinity of cast and printed 30 and 50 wt% PPS aerogels. c) Compressive stress versus strain profiles of printed PPS aerogels. d) Compressive modulus versus density plot of cast and printed PPS aerogels. Open green symbols = series of low-density cast aerogels prepared at concentrations ranging from 9.1 to 23.1 wt%.[38] Closed green symbols = 30 and 50 wt% cast aerogel specimen.

be conducted to rigorously study the relationship between heat transfer, number of layers, layer height, layer cross-sectional area and related toolpath time, and the resulting part microstructure.

### 2.4. Comparison of Cast and Printed PPS Aerogel Physical Properties

The physical properties of the printed aerogels were compared to cast aerogels, which act as control samples, to determine any effect of the printing process on density, porosity, and crystallinity of DIW aerogels. Data of 30 and 50 wt% cast PPS aerogels, in addition to data from the authors' previous study, was used to elucidate the effects of printing on aerogel properties.[38] **Figure 4** compares the physical properties of the printed and cast PPS aerogels. Figure 4a shows that, for all aerogels, porosity decreased linearly as polymer concentration of the aerogel (and thus aerogel density) increased, as expected. A linear trendline through all samples, both cast and printed, displays a $R^2$ value of 0.9925, indicating that the printing process has little effect on the density versus porosity relationship of the PPS aerogels. The variability of the density and porosity at each concentration is larger in the printed parts than in the cast parts, likely due to overextrusion/underextrusion deviations, which created imperfect cylinders and slight variations in the volume measurements (and thus the density calculations) of some of the printed parts.

Figure 4b displays the percent crystallinity of the printed aerogels, and compares them to cast analogues at the same compositions. The crystallinity of all four sets of aerogels is high, around 40–44%, suggesting that the TIPS process is useful for creating highly crystalline parts. The difference in crystallinity between cast and printed parts is minimal, suggesting that the printing process does not disrupt nor does it enhance the crystallinity of the aerogel. PPS is not known to be polymorphic, and wide-angle x-ray scattering (WAXS) patterns (Figure S5, Supporting Information) of cast and printed 30 and 50 wt% PPS aerogels display similar features at similar scattering vectors, indicating that printing does not affect the PPS crystal structure. The variation of the crystallinity of the printed parts is larger than those in the cast parts; there are at least two possible explanations for this variation. One explanation is that temperature oscillations in the heated-DIW barrel alters the crystallization window once the solution is extruded, creating additional variability in the crystallinity of the AM parts. Another possibility is that, due to the inconsistent cooling across each layer, some variation in crystallinity is introduced throughout the part. Overall, Figure 4a,b indicates that critical physical properties are generally unperturbed by the printing process, suggesting that heated-DIW with in situ TIPS is a viable processing option for creating complex aerogel parts without sacrificing important properties inherent to the cast aerogels.

### 2.5. Mechanical Behavior of Cast and Printed PPS Aerogels

Mechanical properties of printed PPS aerogels may be tuned through a change in ink formulation. Figure 4c,d reveals the compressive mechanical behavior of printed PPS aerogels. In Figure 4c, compressive stress versus strain curves for each of the individual printed 30 and 50 wt% aerogels are plotted. The

polymer composition, and thus the morphology, of the aerogels greatly impacts their compressive response. The printed 30 wt% aerogels display a typical compressive response for a porous polymeric sample: an initial linear-elastic zone, followed by a yield and a plateau of deformation as members buckle and bend, and finally densification of the porous structure.[59] Interestingly, the printed 50 wt% aerogels show a deformation profile that is very different from a cast part (Figure S5, Supporting Information), but is instead more similar to that of a solid semiductile polymer: an initial linear-elastic region, then a yield point, followed by eventual failure at relatively low strains.[60,61] Figure S6 (Supporting Information) reveals that the stress versus strain profiles of cast 30 and 50 wt% aerogels display very similar cellular solid-like responses. Both 30 and 50 wt% cast PPS aerogels contain axialitic morphologies, which suggests that the origins of the difference in stress versus strain profiles between 30 and 50 wt% DIW aerogels arise from morphological differences rather than compositional differences. The deviation between compressive strengths in the four 50 wt% aerogels (approximately 8.25 MPa between highest and lowest compressive strength) is related to the specific density of each aerogel and not a unique defect generated via printing, as reported in Figure S7 (Supporting Information).

The results in Figure 4c suggest that the difference in morphology between the two sets of aerogels leads to different compressive failure modes. The axialitic morphology of the 30 wt% parts, which forms a robust interconnected network, responds in a fashion similar to traditional porous polymeric bodies,[59] while the spherulitic morphology of the 50 wt% parts fail in a more brittle manner, as there is less intercrystalline connectivity compared to the axialitic morphologies, and the spherulitic interstitial boundaries act as cracks and thus concentrate stress.[61,62] This reveals the importance of control over the nucleation density when applying TIPS technology to a DIW process, as it affects the aerogel microstructure and thus the final part properties.

Figure 4d highlights the modulus versus density relationship of the printed PPS aerogels, and compares those to the cast aerogels. In the printed parts, the moduli increases with composition and trends towards the modulus of bulk PPS (3.4 GPa),[30] indicating that heated-DIW printed PPS parts can be constructed with tunable mechanical properties. The 50 wt% parts display much higher moduli ($E_{30\ \mathrm{DIW}} = 33.0 \pm 7.93$ MPa; $E_{50\ \mathrm{DIW}} = 106.5 \pm 24.0$ MPa), but much lower ductility ($\epsilon_{\mathrm{break,30\ DIW}} = 0.725 \pm 0.026$ mm mm$^{-1}$; $\epsilon_{\mathrm{break,50\ DIW}} = 0.323 \pm 0.123$ mm mm$^{-1}$) than the 30 wt% parts. The compressive moduli of the printed PPS aerogels are high compared to other aerogels fabricated via AM,[63–65] and approach the moduli of their cast analogues ($E_{30\ \mathrm{Cast}} = 106.8 \pm 4.9$ MPa; $E_{50\ \mathrm{Cast}} = 360.5 \pm 28.4$ MPa).

The moduli of the printed parts display more variability than those in the cast aerogels at the same compositions (30 and 50 wt%). Variations in density and crystallinity, in addition to the presence of defects and layer interfaces could explain this variability. A scaling law, $n$, of 2.78 was fit through the cast aerogel samples indicating good strut interconnectivity, between that of an ideal cellular solid ($n = 2$) and a poorly connected mass fractal system ($n = 3.6$).[38] While the modulus increase for the printed 30 and 50 wt% aerogels parallels the scaling observed for the cast aerogels, the morphological differences between the printed aerogels diminishes the physical significance of a power law relationship of modulus versus density for these samples. In general, the ability of the printed gels to maintain a high percentage of the mechanical behavior of the cast aerogels indicates the efficacy of printing PPS TIPS solutions via heated-DIW.

## 3. Conclusion

In this work, the printing of PPS aerogels was realized for the first time via a unique integration of heated MEX and a TIPS process to rapidly solidify the printed roads. Fabrication of a heated extruder allowed for printing of PPS/DPA solutions into solvated gels which were subsequently processed into PPS aerogels. These new structures are otherwise unprintable via commercially available AM methods. In this approach, PPS was first gelled in DPA to create two concentrations of inks; those feedstocks were dissolved in the heated extruder forming a solution, which was then extruded using pneumatic pressure into discrete roads. Upon deposition, printed roads solidified rapidly via the TIPS process. Solvated gel parts were built in a layer-wise fashion, and upon solvent extraction the printed aerogels were formed. This work presents a pathway for printing aerogels from PPS and other high performance thermoplastics which can undergo TIPS.

Large thermal gradients between the nozzle and the print environment lead to fast PPS crystallization and thus rapid printed road solidification, allowing for time-efficient printing of multilayer solvated gel parts. Cooling and solidification behavior was confirmed through correlation between in situ IR camera video and the thermal transitions of PPS/DPA solutions via DSC. Multiple complex architectures were printed involving sharp corners and rounded curvature, infill, and many stacked layers. The gel microstructure was observed to change with polymer composition, likely due to the self-nucleation behavior of PPS. Through the printing parameters used in this study, the 30 wt% PPS aerogels displayed axialitic morphologies, while 50 wt% aerogels displayed spherulitic morphologies. Porosity, density, and the crystallinity of the aerogels followed the same trend as cast aerogels, indicating that the printing process does not greatly impart unique defects on the physical nature of the aerogels as compared to their cast analogues. Compressive properties of the printed aerogels changed with composition and also with aerogel morphology, suggesting that control of printing conditions can have a significant impact on final part properties. Importantly, printed PPS aerogels display improved compressive moduli over previously reported DIW-printed aerogels,[63–65] providing a new alternative when robust, geometrically complex, solvent-resistant, and thermally stable aerogels are desired.

Given the compositionally dependent morphology of the printed parts (e.g., axialitic versus spherulitic), it is anticipated that control of this behavior could be leveraged in the future to create parts with gradient microstructures. Parts requiring areas of designed failure (such as a crumple zone in an automobile) could be printed at higher temperatures, yielding spherulitic morphologies with brittle mechanical response (see Figure 4c), without sacrificing density, porosity, crystallinity, or surface area. These zones could be reinforced by aerogel made of an axialitic microstructure featuring increased ductility and strain-at-break. Future studies investigating the interrelationships between printing temperature, ink composition, morphology, and mechanical response could allow greater, and even in situ, control over these designed failure and reinforcement zones. Investigation of the

heat transfer within a printed part as a function of the number of layers, layer height, and pause time between layer prints will also allow for a deeper understanding of the complex formation of layer interfaces. Probing the effects of PPS gel microstructure on additional properties such as thermal conductivity, absorption or filtration of specific pollutants, and acoustic behavior will allow for expanded applications of printed aerogels. Also, use of a pressure cell attachment to a parallel plate rheometer could allow for the rheology of PPS/DPA inks to be measured in a sealed environment, where vital relationships between temperature, shear rate, and flow behavior could be studied. Overall, printed PPS aerogels are mechanically robust and highly porous, and feature tailorable properties based on the initial ink concentration and printing parameters.

## 4. Experimental Section

*Materials*: PPS (Ryton QA 200N) was provided by Solvay Specialty Polymers (Alpharetta, GA), and DPA)(99.0%) was purchased from Oakwood Chemical (Estill, SC) and Sigma-Aldrich Inc. (St. Louis, MO). Ethanol (200 proof, 100%, USP, Decon Labs) was purchased from Fisher Scientific Company (Pittsburgh, PA). All polymers and chemicals were used as-received.

*PPS/DPA Gel Ink Formulation*: Ink feedstocks (PPS/DPA gels) were fabricated in a similar fashion as reported by Godshall et al.[38] Briefly, PPS and solid DPA ($T_m$ = 32–34 °C) were premixed at the proper mass ratios (either 30 or 50 wt% PPS for this study) inside of large test tubes, sealed, and purged with Argon gas for at least 15 min to remove air and decrease potential oxidation of the solution, which may occur to PPS and/or DPA at elevated temperatures.[66] The mixture was then heated to 270 °C inside of a metal bath whereby the DPA dissolved the PPS after 20–60 min depending on the concentration. Once the polymer was dissolved, the mixture was stirred vigorously for 5–10 min to homogenize the solution. After homogenization, the solution was removed from the metal bath and allowed to cool to room temperature under ambient conditions. Upon cooling, the solution phase separated and formed an opaque, solidified gel in 2–3 min. The room temperature gel was removed from the test tube and cut into smaller pellet-sized pieces, ready for loading into the heated-DIW extruder barrel.

*Heated-DIW Printing*: To enable simultaneous DIW-TIPS printing, a 3-axis gantry was constructed and outfitted with a customized heated DIW barrel, displayed in Figure S8 (Supporting Information). This custom extruder was designed to meet the need for high temperatures (>215 °C) while also being resistant to solvents. As opposed to a plunger based DIW extruder that would require chemically and thermally stable seals, a simple pneumatically actuated extruder was chosen and designed with Schedule 80 stainless steel fittings capable of resisting the elevated pressures at temperatures well above 200 °C. The Schedule 80 stainless steel barrel contains two heating zones. An upper heating zone, powered by an insulated band heater, prevented excess heat loss from the hot end, and reduced clogging in the upper portion of the extruder. The lower heating zone, which dissolved the gel ink into a homogenous solution, was powered via a second insulated band heater. The temperatures of both heating zones were controlled by independent J-KEM Model 210 temperature controllers; thermocouples were attached onto the upper barrel and onto the brass extrusion nozzle to monitor the temperature in each zone. Pneumatic pressure was supplied to the extruder via a Nordson Ultimus V system, using argon gas instead of compressed air to reduce potential oxidative degradation of the polymer solution at high temperatures. A wooden build plate was used as the printing substrate, as the deposited PPS/DPA ink adhered well to its surface, yet the completed part was still easily removed after printing.

For determination of proper printing temperatures, the upper heating zone was set to 125 °C during all printing. Temperature and pressure parameters were selected that produced a consistent extrudate that remelted previous layers and did not lead to degradation of the polymer solution. The lower heating band controlled the temperature needed to enable a consistent flow (i.e., extrudate temperature was measured by IR camera to be 208 ± 8 °C and 243 ± 8 °C for the 30 and 50 wt% solutions, respectively). Full printing parameters are presented in Table S1 (Supporting Information).

For both ink formulations, a 0.4 mm diameter nozzle was used to deposit layer heights of 0.5 mm at an extrusion speed of 4.0 mm $s^{-1}$. Due to imperfect barrel insulation and the nature of PID controlled heating, slight oscillations in temperature during printing lead to transiently varying viscosity and thus a need for minor pressure modulation during extrusion. Existing DIW analytical models for predicting optimal extrusion pressures of PPS/DPA inks were not sufficient since the experimental set up could not allow for the exact non-Newtonian viscosity of the ink to be measured in its solution state. For the 30 wt% ink, an average extrusion pressure of 2 psi was used; for the 50 wt% ink, an average extrusion pressure of 6 psi was used.

*PPS Aerogel Postprocessing*: Printed aerogels were allowed to cool to room temperature, then were submerged in 50 °C ethanol for 4 days to extract DPA. Next, the ethanol-containing organogels were submerged in deionized water at room temperature for 4 days to create hydrogels. During these solvent exchange processes, the ethanol and water were refreshed daily. The hydrogels were then frozen at −18 °C overnight and freeze dried using a LabConco lyophilizer to yield printed PPS aerogels.

*Printed Part Characterization*: In situ IR camera videos of DIW printing were taken using a Micro-Epsilon thermoIMAGER TIM 640 infrared camera. The TIMConnect Software was used to record video and collect simultaneous spatial, temporal, and thermal data.

The density of printed hollow cylindrical aerogel samples was measured by dividing the mass of each part by its measured volume. True part volume was calculated directly using the measured dimensions of each printed aerogel cylinder. Nominal cylinder dimensions were: a height of 10 mm, an outer radius of 5 mm and an inner radius of 4 mm (yielding an approximate wall thickness of 1 mm). Four replicate parts of each printed polymer composition were measured.

Porosity of printed hollow cylindrical aerogel samples was measured using a Micromeritics AccuPyc II 1340 helium pycnometer, according to ASTM D6226-21.[67] A 3.5 $cm^3$ insert and an equilibration rate of 0.03 psig $min^{-1}$ were used. To calculate porosity, the following equation was used:

$$P = \left[\frac{(V - V_{spec})}{V}\right] \times 100 \quad (1)$$

where $P$ is the volumetric porosity (%), $V$ is the hollow cylinder volume, and $V_{spec}$ is the skeletal density. Four replicate parts of each printed polymer composition were measured. In addition, nitrogen porosimetry was carried out on an Anton Paar Autosorb iQ C-XR adsorption analyzer to calculate (BET) surface areas of printed and cast PPS aerogels.

The morphology of printed aerogels was analyzed via a Zeiss LEO 1550 field-emission SEM (FE-SEM) with in-lens detection. Parts were freeze-fractured and mounted on carbon tape, then sputter coated with 5 nm of Iridium using a Leica EM ACE600 sputter coater. Image analysis of SEM micrographs was performed using the ImageJ image processing software.

The degree of crystallinity of the solvent extracted PPS aerogels was measured using first-heat scans (10 °C $min^{-1}$ from 40 °C to 330 °C) from a TA Instruments Q2000 DSC. Percent crystallinity (%$X_c$) was calculated via:

$$\%X_c = \left(\frac{\Delta H_m}{\Delta H_m^o}\right) \times 100 \quad (2)$$

where $\Delta H_m$ is the measured heat of fusion, taken as the integrated area under the melting peak, and $\Delta H_m°$ is the theoretical heat of fusion of 100% crystalline PPS, equal to 111.7 J $g^{-1}$.[68]

Thermogravimetric analysis (TGA) using a TA Instruments Discovery 550 TGA was performed on printed PPS/DPA samples to measure

DPA content and to confirm complete removal of DPA in the solvent extracted aerogels. Heating ramps were performed from room temperature to 850 °C at 20 °C $min^{-1}$ in a nitrogen environment.

WAXS experiments were conducted at beamline 9-ID-C at the Advanced Photon Source (APS) at Argonne National Labs (Lemont, IL).[69,70] The Nika macro for Igor Pro was utilized to develop WAXS data.[71]

To measure the compressive properties of the printed cylindrical aerogels, an Instron 3340 Universal Testing System was equipped with compressive platens, a 5 kN load cell, and a crosshead speed of 1 mm $min^{-1}$. Four replicate parts of each polymer composition were measured.

Cast aerogels were fabricated according to the process outlined in Godshall et al.[38] 30 and 50 wt% cast aerogels were tested according to the same methods as outlined above (density, porosity, SEM, BET, DSC, and uniaxial compression).

In order to tune printing parameters and optimize the printing process, the rheological properties of DIW inks are often studied. Due to the close proximity of the melting temperature of the PPS/DPA solvated gel inks ($T_{m,\,30\,wt\%}$ = 243.9 °C, $T_{m,\,50\,wt\%}$ = 253.3 °C, Figure S9, Supporting Information) and the pure DPA boiling point ($T_{b,\,DPA}$ = 330 °C), solvent evaporation was inevitable during rheological testing. While the ink in the extruder barrel is ideally sealed off from the environment, the material between the parallel plates is not; excess evaporation in the rheometer prevented accurate characterization of the shear thinning behavior and solidification/dissolution transition temperatures of the inks that occur during the printing process. Qualitatively, however, the 50 wt% ink was noticeably more viscous than the 30 wt% ink, and Figure S9 (Supporting Information) indicates that the 50 wt% ink also has a higher melting point. The increase in viscosity with increasing polymer concentration was also reflected in the extrusion pressure required to print each ink, with the 30 wt% ink (2 psi) requiring a lower pressure than the 50 wt% ink (6 psi) (Table S1, Supporting Information). Importantly, the quantity of solvent that may have evaporated during the printing process should be determined, to confirm that the ink concentration remains consistent during and after printing. The nozzle is the only escape point for vapors during printing, and ideally solvent loss should be kept to a minimum to maintain a constant ink composition. Figure S10 (Supporting Information) highlights TGA degradation curves that quantify the amount of DPA remaining in solvated printed parts. In a 50 wt% printed part, 46.6% of the solvent is retained, indicating that the solvent content in the printed part was approximately equal to that in the precursor ink, suggesting that solvent evaporation was not an issue during heated-DIW of PPS/DPA inks.

*Statistical Analysis*: Data presented as mean ± SD, $n = 4$ for printed aerogels and $n = 5$ for cast aerogels, unless otherwise stated.

## Supporting Information

Supporting Information is available from the Wiley Online Library or from the author.

## Acknowledgements

G.F.G. and D.A.R. contributed equally to this work. This material is based upon work supported by the National Science Foundation under Grant Nos. DMR-1809291 and DMR-2104856. This research used resources of the Advanced Photon Source, a U.S. Department of Energy (DOE) Office of Science user facility operated for the DOE Office of Science by Argonne National Laboratory under Contract No. DE-AC02-06CH11357. WAXS data was collected on the 9-ID-C beamline at the APS, Argonne National Laboratory.

## Conflict of Interest

The authors declare no conflict of interest.

## Data Availability Statement

The data that support the findings of this study are available from the corresponding author upon reasonable request.

## Keywords

additive manufacturing, hierarchical porosity, material extrusion, polymer aerogel, polyphenylene sulfide, thermally induced phase separation

Received: August 5, 2023
Revised: October 30, 2023
Published online:

[1] C. I. Idumah, A. C. Ezika, V. U. Okpechi, *Surf. Interfaces* **2021**, *25*, 101258.
[2] P. Paraskevopoulou, D. Chriti, G. Raptopoulos, G. C. Anyfantis, *Materials* **2019**, *12*, 1543.
[3] S. S. Kistler, *Nature* **1931**, *127*, 741.
[4] S. Zhao, W. J. Malfait, N. Guerrero-Alburquerque, M. M. Koebel, G. Nystrom, *Angew. Chem., Int. Ed.* **2018**, *57*, 7580.
[5] X. Jiang, R. Du, R. Hübner, Y. Hu, A. Eychmüller, *Matter* **2021**, *4*, 54.
[6] H. Tetik, Y. Wang, X. Sun, D. Cao, N. Shah, H. Zhu, F. Qian, D. Lin, *Adv. Funct. Mater.* **2021**, *31*, 2103410.
[7] J. L. Gurav, I.-K. Jung, H.-H. Park, E. S. Kang, D. Y. Nadargi, *J. Nanomater.* **2010**, *2010*, 409310.
[8] Y. Li, B. Ma, R. Zhang, X. Luo, *Polymer* **2022**, *253*, 125035.
[9] X. Sun, T. Fujimoto, H. Uyama, *Polym. J.* **2013**, *45*, 1101.
[10] Y. Guo, T. Zhang, M. Chen, C. Li, H. Wu, S. Guo, *J. Membr. Sci.* **2021**, *619*, 118778.
[11] I. Gibson, D. Rosen, B. Stucker, M. Khorasani, *Additive Manufacturing Technologies*, Springer International Publishing, Cham **2021**.
[12] B. G. Compton, J. A. Lewis, *Adv. Mater.* **2014**, *26*, 5930.
[13] M. Vaezi, H. Seitz, S. Yang, *Int. J. Adv. Manuf. Technol.* **2013**, *67*, 1721.
[14] D. A. Rau, J. Herzberger, T. E. Long, C. B. Williams, *ACS Appl. Mater. Interfaces* **2018**, *10*, 34828.
[15] C. B. Arrington, D. A. Rau, C. B. Williams, T. E. Long, *Polymer* **2021**, *212*, 123306.
[16] C. Xu, B. Quinn, L. L. Lebel, D. Therriault, G. L'Espérance, *ACS Appl. Mater. Interfaces* **2019**, *11*, 8499.
[17] A. Shahzad, I. Lazoglu, *Composites, Part B* **2021**, *225*, 109249.
[18] J. W. Boley, K. Chaudhary, T. J. Ober, M. Khorasaninejad, W. T. Chen, E. Hanson, A. Kulkarni, J. Oh, J. Kim, L. K. Aagesen, A. Y. Zhu, F. Capasso, K. Thornton, P. V. Braun, J. A. Lewis, *Adv. Mater.* **2017**, *29*, 1604778,.
[19] S. Ji, M. Guvendiren, *Front. Bioeng. Biotechnol.* **2017**, *5*, 23.
[20] M. A. S. R. Saadi, A. Maguire, N. T. Pottackal, M. S. H. Thakur, M. M. Ikram, A. J. Hart, P. M. Ajayan, M. M. Rahman, *Adv. Mater.* **2022**, *34*, 2108855.
[21] S. S. L. Chan, R. M. Pennings, L. Edwards, G. V. Franks, *Addit. Manuf.* **2020**, *35*, 101335.
[22] P. J. Scott, D. A. Rau, J. Wen, M. Nguyen, C. R. Kasprzak, C. B. Williams, T. E. Long, *Addit. Manuf.* **2020**, *35*, 101393.
[23] O. Rios, W. Carter, B. Post, P. Lloyd, D. Fenn, C. Kutchko, R. Rock, K. Olson, B. Compton, *Mater. Today Commun.* **2018**, *15*, 333.
[24] S.-Z. Guo, M.-C. Heuzey, D. Therriault, *Langmuir* **2014**, *30*, 1142.
[25] S.-Z. Guo, F. Gosselin, N. Guerin, A.-M. Lanouette, M.-C. Heuzey, D. Therriault, *Small* **2013**, *9*, 4118.
[26] S. Chandrasekaran, B. Yao, T. Liu, W. Xiao, Y. Song, F. Qian, C. Zhu, E. B. Duoss, C. M. Spadaccini, Y. Li, M. A. Worsley, *Mater. Horiz.* **2018**, *5*, 1166.

[27] B. Yao, H. Peng, H. Zhang, J. Kang, C. Zhu, G. Delgado, D. Byrne, S. Faulkner, M. Freyman, X. Lu, M. A. Worsley, J. Q. Lu, Y. Li, *Nano Lett.* **2021**, *21*, 3731.
[28] H. C. Liu, A. D. Auguste, J. O. Hardin, A. Sharits, J. D. Berrigan, *ACS Appl. Mater. Interfaces* **2021**, *13*, 27364.
[29] A. D. Luca, J. R. d. Wijn, C. A. v. Blitterswijk, S. Camarero-Espinosa, L. Moroni, *Macromol. Rapid Commun.* **2017**, *38*, 1700186.
[30] *Ryton QA200N Polyphenylene Sulfide Technical Data Sheet*, Solvay, **2020**. [Online]. Available: https://www.matweb.com/search/datasheet.aspx?matguid=fed1d60725244d9ba944875f7c0891dd&ckck=1
[31] H. N. Beck, *J. Appl. Polym. Sci.* **1992**, *45*, 1361.
[32] A. S. Rahate, K. R. Nemade, S. A. Waghuley, *Rev. Chem. Eng.* **2013**, *29*, 471.
[33] P. Zuo, A. Tcharkhtchi, M. Shirinbayan, J. Fitoussi, F. Bakir, *Macromol. Mater. Eng.* **2019**, *304*, 1800686.
[34] M. Q. Ansari, M. J. Bortner, D. G. Baird, *Addit. Manuf.* **2019**, *29*, 100814.
[35] P. Yeole, A. A. Hassen, S. Kim, J. Lindahl, V. Kunc, A. Franc, U. Vaidya, *Addit. Manuf.* **2020**, *34*, 101255.
[36] C. A. Chatham, T. E. Long, C. B. Williams, *Addit. Manuf.* **2019**, *28*, 506.
[37] C. A. Chatham, T. E. Long, C. B. Williams, *MRS Commun.* **2021**, *11*, 179.
[38] G. F. Godshall, G. A. Spiering, E. R. Crater, R. B. Moore, *ACS Appl. Polym. Mater.* **2023**, *5*, 7994.
[39] S. J. Talley, X. Yuan, R. B. Moore, *ACS Macro Lett.* **2017**, *6*, 262.
[40] S. J. Talley, C. L. AndersonSchoepe, C. J. Berger, K. A. Leary, S. A. Snyder, R. B. Moore, *Polymer* **2017**, *126*, 437.
[41] S. J. Talley, S. L. Vivod, B. A. Nguyen, M. B. Meador, A. Radulescu, R. B. Moore, *ACS Appl. Mater. Interfaces* **2019**, *11*, 31508.
[42] A. Elhaj, K. Irgum, *ACS Appl. Mater. Interfaces* **2014**, *6*, 15653.
[43] R. Zeinali, L. J. d. Valle, J. Torras, J. Puiggali, *Int. J. Mol. Sci.* **2021**, *22*, 3504.
[44] D. R. Lloyd, S. S. Kim, K. E. Kinzer, *J. Membr. Sci.* **1991**, *64*, 1.
[45] S. S. Kim, D. R. Lloyd, *J. Membr. Sci.* **1991**, *64*, 13.
[46] D. R. Lloyd, K. E. Kinzer, H. S. Tseng, *J. Membr. Sci.* **1990**, *52*, 239.
[47] Y. Furushima, M. Nakada, Y. Yoshida, K. Okada, *Macromol. Chem. Phys.* **2018**, *219*, 1700481.
[48] X. Gao, S. Qi, X. Kuang, Y. Su, J. Li, D. Wang, *Addit. Manuf.* **2021**, *37*, 101658.
[49] M. Zhou, B. Chen, Y. Li, J. Jiang, W. Zhai, *Adv. Eng. Mater.* **2023**, *25*, 2201468.
[50] C. A. Chatham, C. E. Zawaski, D. C. Bobbitt, R. B. Moore, T. E. Long, C. B. Williams, *Macromol. Mater. Eng.* **2019**, *304*, 1800764.
[51] H.-h. Lin, Y.-h. Tang, T.-y. Liu, H. Matsuyama, X.-l. Wang, *J. Membr. Sci.* **2016**, *507*, 143.
[52] M. Trujillo, M. L. Arnal, A. J. Müller, M. A. Mujica, C. Urbina de Navarro, B. Ruelle, P. Dubois, *Polymer* **2012**, *53*, 832.
[53] C.-Y. Chiang, D. R. Lloyd, *J. Porous Mater.* **1996**, *2*, 273.
[54] L. Sangroniz, D. Cavallo, A. J. Muller, *Macromolecules* **2020**, *53*, 4581.
[55] P. Yan, F. Yang, M. Xiang, T. Wu, Q. Fu, *Polymer* **2020**, *195*, 122439.
[56] S. Hu, F. Yang, M. Xiang, Y. Cao, T. Wu, Q. Fu, *Polymer* **2022**, *262*, 125427.
[57] N. P. Levenhagen, M. D. Dadmun, *ACS Appl. Polym. Mater.* **2019**, *1*, 876.
[58] S. Farzaneh Kalourazi, F. Wang, H. Zhang, M. Selzer, B. Nestler, *J. Phys.: Condens. Matter* **2022**, *34*, 444003.
[59] M. F. Ashby, *Metall. Mater. Trans. A* **1983**, *14A*, 1755.
[60] I. M. Ward, J. Sweeney, *Mechanical Properties of Solid Polymers*, Wiley, Chichester, West Sussex, UK **2012**.
[61] J. L. Way, J. R. Atkinson, J. Nutting, *J. Mater. Sci.* **1974**, *9*, 293.
[62] A. Lustiger, C. N. Marzinsky, R. R. Mueller, *J. Polym. Sci., Part B: Polym. Phys.* **1998**, *36*, 2047.
[63] S. Camarero-Espinosa, M. Carlos-Oliveira, H. Liu, J. F. Mano, N. Bouvy, L. Moroni, *Adv. Healthcare Mater.* **2022**, *11*, 2101415.
[64] V. C. F. Li, A. Mulyadi, C. K. Dunn, Y. Deng, H. J. Qi, *ACS Sustainable Chem. Eng.* **2018**, *6*, 2011.
[65] L. Huang, X. Du, S. Fan, G. Yang, H. Shao, D. Li, C. Cao, Y. Zhu, M. Zhu, Y. Zhang, *Carbohydr. Polym.* **2019**, *221*, 146.
[66] P. Yan, W. Peng, F. Yang, Y. Cao, M. Xiang, T. Wu, Q. Fu, *Polym. Degrad. Stab.* **2022**, *197*, 109863.
[67] *D6226-21 Standard Test Method for Open Cell Content of Rigid Cellular Plastics*, ASTM International, PA, USA **2021**.
[68] P. Huo, P. Cebe, *Colloid Polym. Sci.* **1992**, *270*, 840.
[69] J. Ilavsky, P. R. Jemian, A. J. Allen, F. Zhang, L. E. Levine, G. G. Long, *J. Appl. Crystallogr.* **2009**, *42*, 469.
[70] J. Ilavsky, F. Zhang, A. J. Allen, L. E. Levine, P. R. Jemian, G. G. Long, *Metall. Mater. Trans. A* **2013**, *44*, 68.
[71] J. Ilavsky, *J. Appl. Crystallogr.* **2012**, *45*, 324.